Journal of Computational Physics **170,** 161–183 (2001)
doi:10.1006/jcph.2001.6731, available online at http://www.idealibrary.com on IDEAL®

Adaptive Limiters for Improving the Accuracy of the MUSCL Approach for Unsteady Flows

G. Billet and O. Louedin

ONERA, B.P. 72-29, av. de la Division Leclerc, 92322 Châtillon Cedex, France
E-mail: billet@onera.fr

Received November 15, 1999; revised January 19, 2001

An improvement in the accuracy of the MUSCL approach is based on the use of AUSM splitting and a triad of limiters defined by the behavior of each physical quantity. Some test cases are shown.

Key Words: MUSCL approach; TVD schemes; Euler equations; Navier–Stokes equations.

1. INTRODUCTION

The simulations of severe flow conditions, such as in unsteady reactive or supersonic flows, require robust numerical methods. Many computations use a class of algorithms based either on flux vector splitting (VS) or on flux difference splitting (DS). Liou and Steffen [9] have proposed a remarkably simple upwind VS. This splitting, called AUSM, treats the convective and pressure terms separately. The convective quantities are upwind-biased extrapolated to the cell interface using a properly defined cell face advection Mach number. AUSM keeps the qualities of VS (robustness and efficiency) and recovers the accuracy attributed to DS. To capture strong and/or rapid physical fluctuations accurately, the local variation of each quantity has to be incorporated as much as possible in the writing of the scheme. For instance, ENO schemes choose the stencil which provides the most regular solution in order to minimize numerical over- and undershoots. In this paper, we take the limiter which minimizes the numerical error terms (dissipative and dispersive terms) following the local evolution of quantities. To improve efficiency, the equivalent system (ES) needs to be studied, including the expression for the slope limiters. Their expressions are controlled by both the local and the surrounding physical variation of the quantities. For each quantity, six different cases are considered, each associated with a different physical variation. A triad of limiters is defined, which minimizes or cancels the second-order truncation errors. From this study, a new explicit scheme is written. Compared to a common TVD-MUSCL scheme, it is not complicated and gives a more precise solution.

0021-9991/01 $35.00

This scheme is applied to 1-D, 2-D, and 3-D test cases. The results show that we obtain a good accuracy compared to ENO or Hermitian schemes.

2. FLUX SPLITTINGS AND MUSCL APPROACH

The hyperbolic part of the conservation form of the 1-D Navier–Stokes equations is classically written as

$$\begin{aligned} &V_t + f_x = 0 \quad \text{with} \quad V = \begin{bmatrix} \rho \\ \rho u \\ \rho E \end{bmatrix}, \quad f = \begin{bmatrix} \rho u \\ \rho u^2 + p \\ \rho u H \end{bmatrix}, \\ &V(x,0) = V^0(x), \quad -\infty < x < +\infty, \quad t \geq 0. \end{aligned} \tag{1}$$

The equation of state is $p = \rho RT$. ρ, u, p, T, R, E, and H are, respectively, the density, the velocity, the static pressure, the temperature, the universal gas constant, the total energy, and the total enthalpy per unit of volume. In discrete form, (1) is expressed as

$$\begin{aligned} V_j^{n+1} &= V_j^n - \sigma\left(F_{j+\frac{1}{2}} - F_{j-\frac{1}{2}}\right), \\ V_j^n &= V\left(U_j^n\right), \quad \sigma = \Delta t/\Delta x, \quad F_{j+\frac{1}{2}} = F\left(U_{j-1}^n, U_j^n, U_{j+1}^n, U_{j+2}^n\right), \end{aligned} \tag{2}$$

where F is a numerical flux which has to verify $F(U,\ldots,U) = f(V)$, and $U_j^n = U_j$ is a set of physical quantities defined at time $n\Delta t$ and at grid point $j\Delta x$. Δx is assumed to be constant and Δt is related to Δx by the CFL condition. With the MUSCL approach [21], the backward and forward extrapolated values of $U_{j+(1/2)}$ at the interface $j + \frac{1}{2}$ can be written as

$$\begin{aligned} U_{j+1/2}^L &= L(U_{j-1}, U_j, U_{j+1}) = U_j + \frac{\varphi_1(r_j)}{2}(U_{j+1} - U_j), \\ U_{j+1/2}^R &= R(U_j, U_{j+1}, U_{j+2}) = U_{j+1} - \frac{\varphi_2^R\left(\frac{1}{r_{j+1}}\right)}{2}(U_{j+1} - U_j). \end{aligned} \tag{3}$$

At the interface $j - \frac{1}{2}$, we have

$$\begin{aligned} U_{j-1/2}^L &= L(U_{j-2}, U_{j-1}, U_j) = U_{j-1} + \frac{\varphi_2^L(r_{j-1})}{2}(U_j - U_{j-1}), \\ U_{j-1/2}^R &= R(U_{j-1}, U_j, U_{j+1}) = U_j - \frac{\varphi_1\left(\frac{1}{r_j}\right)}{2}(U_j - U_{j-1}), \end{aligned}$$

where φ_1 and $\varphi_2^{L,R}$ are nonlinear functions of $r_j = (U_j - U_{j-1})/(U_{j+1} - U_j)$. The nonlinear interpolations L and R have to verify the following properties (P_1): homogeneity, translation invariance, left–right symmetry, and convexity [20].

The flux $F_{j+(1/2)}$ is written in the general form

$$F_{j+1/2} = F\left(U_{j+1/2}^L, U_{j+1/2}^R\right) - \Phi\Delta G,$$

where

$$\Phi\Delta G = \Phi\left[G\left(U^R_{j+(1/2)}\right) - G\left(U^L_{j+(1/2)}\right)\right]$$

is a dissipation term. We are more interested in the primitive form of AUSM splitting. If we define

$$M = F^+_M + F^-_M = \left[\frac{(M^L+1)^2}{4}\right] + \left[-\frac{(M^R-1)^2}{4}\right],$$

$$\begin{bmatrix}0\\p\\0\end{bmatrix} = F^+_a + F^-_a = \begin{bmatrix}0\\ p^L\left(\frac{1+M^L}{2}\right) + p^R\left(\frac{1-M^R}{2}\right)\\0\end{bmatrix}, \quad F^{L,R}_c = \begin{bmatrix}\rho c\\ \rho cu\\ \rho cH\end{bmatrix}^{L,R},$$

then this splitting can be written, at the grid point $j+(1/2)$ and for $-1 \le M \le 1$, as

$$\begin{aligned} F(U^L, U^R) &= (F^+_M + F^-_M)F_c + F^+_a + F^-_a \\ \Phi &= |M|, \quad \Delta G = \frac{1}{2}\left[F^R_c - F^L_c\right], \quad F_c = \frac{F^L_c + F^R_c}{2}, \end{aligned} \tag{4}$$

where M and c represent the Mach number and the speed of sound, respectively. It is possible to take different expressions for U. Generally, it is advantageous to apply the MUSCL approach to the natural quantities. Because our aim, in the future, is the study of the unsteady reactive flows where the temperature T changes rapidly and where the specific heats C_p and C_V depend strongly on T (reactive flows, for example), it seems logical to choose

$$U = [\,\rho, u, T\,]^T.$$

The analysis of ES, also called *modified equations* [11, 14], obtained from Taylor expansions, quantifies the truncation error of the discrete form as Δx and $\Delta t \to 0$. U and F are assumed to be differentiable functions of C^4. For each component U_i, the expansions reflect the surrounding physical behavior associated with the specific approach used here. Six different cases are considered for each component U_i (Fig. 1):

$$\text{no extremum at } j \begin{bmatrix} \text{case 1: monotonic evolution} \\ \text{case 2: extremum at the nodes } j-1 \text{ and } j+1 \\ \text{case 3: extremum at the node } j-1 \text{ or } j+1 \end{bmatrix},$$

$$\text{extremum at } j \begin{bmatrix} \text{case 4: no extremum at the nodes } j-1 \text{ and } j+1 \\ \text{case 5: extremum at the nodes } j-1 \text{ and } j+1 \\ \text{case 6: extremum at the node } j-1 \text{ or } j+1 \end{bmatrix}.$$

The different cases considered above may be associated with physical phenomena having different wavenumbers k and therefore may be linked with a range of wavenumbers or a

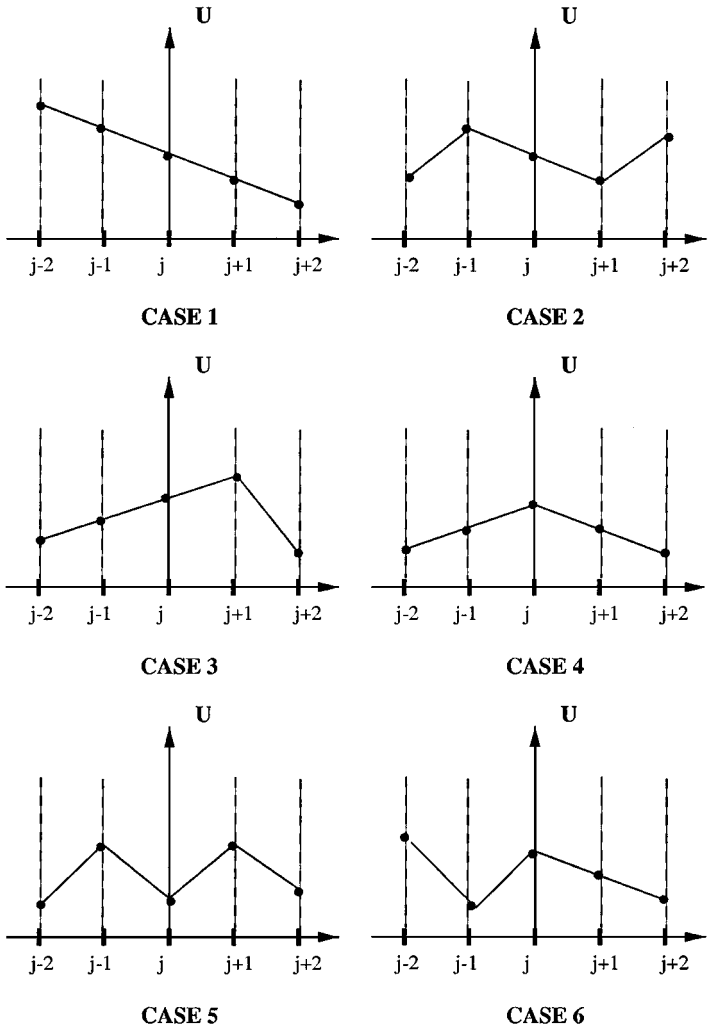

FIG. 1. Different cases associated with the local physical fluctuations.

single wavenumber:

$$\text{case } 1 \leftrightarrow 0 \leq k \leq \frac{\pi}{4\Delta x}$$

$$\text{case } 2 \leftrightarrow k = \frac{2\pi}{3\Delta x} \text{ or } k = \frac{\pi}{2\Delta x}$$

$$\text{case } 3 \leftrightarrow \frac{\pi}{2L} \leq k \leq \frac{\pi}{2\Delta x} (L = \text{length of the domain})$$

$$\text{case } 4 \leftrightarrow \frac{\pi}{2L} \leq k \leq \frac{\pi}{2\Delta x}$$

$$\text{case } 5 \leftrightarrow k = \frac{\pi}{\Delta x}$$

$$\text{case } 6 \leftrightarrow k = \frac{2\pi}{3\Delta x}.$$

In this approach, the goal is to keep the primitive qualities of the schemes (in particular the shock-capturing property or the solving of stiff phenomena) and, at the same time, to

represent, as much as possible, the unsteady or turbulent fluctuations. Therefore, sufficiently strong constraints are applied in some cases but, in others for example, the constraints are weaker in order to develop and not to inhibit the energy cascade for the turbulent flows. From these conditions, in addition to properties (P_1), new basic conditions on φ at the node j are defined:

(1) To keep the TVD property for cases 4, 5, and 6, the value of a local minimum is nondecreasing and the value of a local maximum is nonincreasing (property (P_2)).

(2) A new extremum may appear at node j when an extremum already exists in the environs of node j, to expand the energy cascade and to jump from the wavenumber k to the wavenumber $2k$. Therefore, the least dissipative scheme will be applied to cases 2 and 3 (property (P_3)).

(3) When the evolution is monotonic (case 1), the scheme has to keep the TVD property and to have an accuracy as high as possible (property (P_4)).

In general, to avoid nonmonotonic behaviors when the sign of the physical variation changes, it is assumed that

$$r < 0, \quad \varphi_\alpha = \varphi'_\alpha = 0, \quad (\alpha = 1, 2) \text{ (property } (P_5)).$$

The expressions of φ come from properties $(P_1), \ldots, (P_5)$ and from the study of the ES. This study permits minimization of the dispersive and dissipative error terms produced by the scheme. Property (P_5) does not allow extension of this study based on Taylor expansions to cases 2 and 3 and, consequently, the theoretical results based on analysis of the error terms concern cases 1, 4, 5, and 6 only.

3. FIRST-ORDER ERROR TERMS IN SPACE

Taylor expansions can be made if the condition at the node j,

$$\left|U_i^R - U_i^L\right| \ll \text{Max}\left(\left|U_i^R\right|, \left|U_i^L\right|\right), \quad (i = 1, \ldots, 3),$$

is assumed. This says that the jump at the interface j is considered to be weak (the strong discontinuities are excluded from the proof). The case $|U_i^R - U_i^L| \approx \text{Max}(|U_i^R|, |U_i^L|)$ is not considered in this paper, although it may be present in the velocity under certain circumstances, such as when this quantity has strong fluctuations around zero. The expansions are calculated for positive values of M. The expressions for $M < 0$ are obtained by symmetry (g_i^L is replaced by g_i^R and reciprocally).

After calculation of the Taylor expansions of $r(U)$, $\varphi_\alpha(r(U))$ and of the fluxes $\Psi = \Psi(\varphi_\alpha(r(U)))$ with $\Psi = F_M^-, F_M^+, F_c, \ldots$ at the node j for both cases $U_x \neq 0$ and $U_x = 0$ (with $U_{xx} \neq 0$), (1) is transformed into

$$V_t + F_x + \Delta x[A]U_{xx} + O(\Delta x^2) = 0, \tag{5}$$

where $[A]$ is a (3, 3) matrix. The first-order error term in space, for the kth equation (k = 1, 2, 3) of the system (5) and for the splitting (4), can be expressed as

$$\sum_{i=1}^{3} A_{k_i} U_{i_{xx}} = \frac{1}{2} \sum_{i=1}^{3} \left\{ \begin{array}{l} \left(F_{c_k} F_M^{+\prime} + \frac{M+|M|}{2} F_{c_i}^{L\prime} + F_{a_i}^{+\prime}\right)\left[g_i^L\right] \\ -\left(F_{c_k} F_M^{-\prime} + \frac{M-|M|}{2} F_{c_i}^{R\prime} + F_{a_i}^{-\prime}\right)\left[g_i^R\right] \end{array} \right\} U_{i_{xx}}$$

where

$$g^{L,R} = g^{L,R}(\varphi) = \frac{\varphi_1(-1)}{2} + \frac{\varphi_2^{L,R}(3)}{2} - 1 \quad \text{if } U_x = 0,$$
$$g^{L,R} = g^{L,R}(\varphi') = \varphi_2'^{L,R}(1) - \varphi_1'(1) \quad \text{if } U_x \neq 0,$$
$$\varphi' = \frac{d\varphi}{dr}, \quad F^{+\prime} = \frac{dF^+}{dU^L}, \quad F^{-\prime} = \frac{dF^-}{dU^R}, \quad \left(F_c^{L,R}\right)' = \frac{dF_c}{dU^{L,R}}, \ldots.$$

The first-order term cancels if $g^{L,R} = 0$; therefore, when $U_x \neq 0$,

$$\varphi_2'^L = \varphi_2'^R = \varphi_1' \quad \text{for } r = 1; \tag{6}$$

when $U_x = 0$,

$$\varphi_2^L = \varphi_2^R = 2 \quad \text{for } r = 3. \tag{7}$$

The Taylor expansions at node j include the presence of one extremum (cases 4, 5, and 6) or none (case 1) at this point. But they do not take into account whether one extremum exists or not at the neighbors $j-1$ and $j+1$. If there is no extremum associated with $j-1$ and $j+1$ (cases 1 and 4), any additional constraint appears; but if an extremum is present at these points, the scheme accuracy automatically degenerates (cases 5 and 6):

- If $U_x \neq 0$ at node j, condition (6) is easily met if the nodes $j-1$, j, and $j+1$ have no extremum for component U (case 1). In this case, it is sufficient to take the same function in the second-order TVD domain for each point $j-1$, j, $j+1$.
- If $U_x = 0$ at node j, condition (7) is met if $j-1$ and $j+1$ are not associated with an extremum. But this condition is no longer met if there exists at least one extremum at one of the neighbors of j. When wavelength fluctuations are smaller than or equal to $3\Delta x$ (cases 5 and 6) the first-order error term is still present. In this case, the scheme has stronger dissipative properties to damp these fluctuations.

For case 5, where $g^{L,R} = -1$, and for case 6, where $g^L = -1$ and $g^R = 0$, the dissipative matrix is written, when $M \leq 1$,

$$[A] = [A]_c + [A]_a,$$

with

$$[A]_c = -\begin{bmatrix} A_{11} & A_{12} & A_{13} \\ uA_{11} & uA_{12} + \rho A_{11} & uA_{13} \\ HA_{11} & HA_{12} + \rho u A_{11} & HA_{13} + \rho C_p A_{11} \end{bmatrix},$$

where

$$A_{11} = \frac{c}{2}M, \quad A_{12} = \frac{\rho}{2}\left(M\delta_{l5} + \frac{1+M}{2}\delta_{l6}\right), \quad A_{13} = \frac{\rho c}{4T}M(1-M)\left(\delta_{l5} + \frac{\delta_{l6}}{2}\right),$$

$$[A]_a = -\frac{c^2}{2\gamma}\begin{bmatrix} 0 & 0 & 0 \\ \frac{2}{\rho}A_{12} & \frac{\rho}{c}\left(\delta_{l5} + \frac{\delta_{l6}}{2}\right) & \frac{1}{T}\left(A_{12} + \frac{\rho}{4}\delta_{l6}\right) \\ 0 & 0 & 0 \end{bmatrix}.$$

δ_{l5} and δ_{l6} are the Kronecker symbol, $l = 5$ (case 5) or 6 (case 6).

When $M > 1$,

$$[A] = -\begin{bmatrix} A_{11} & \frac{\rho}{2} & 0 \\ uA_{11} + \frac{RT}{2} & 2\rho A_{11} & \frac{\rho}{2}R \\ HA_{11} & \frac{\rho}{2}H + \rho u A_{11} & \rho C_p A_{11} \end{bmatrix}.$$

For case 5, when $M \to 0$, many terms cancel. In particular, the dissipative matrix cancels if there are only density or temperature fluctuations. In this case, a somewhat more complex dissipative function Φ_d in the region of $M \approx 0$ may be introduced [13]. For case 6, the velocity fluctuations, when they exist, avoid use of the function Φ_d since the scheme remains dissipative even for $M = 0$. For both cases, some elements of $[A]$ present a discontinuity at $M = 1$. The improved scheme AUSM$^+$ allows attenuation of this problem [10].

4. SECOND-ORDER ERROR TERMS IN SPACE

If, at node j, the variations of all the components U_i are included in cases 1 and 4, the spatial derivatives are approximated by a second-order scheme in space if φ_α are chosen well. The expressions of φ_α are defined by studying the second-order error term in space. The discrete form of Eq. (1) takes the expression

$$V_t + F_x + \Delta x^2(\chi_1 B U_{xxx} + C U_{xx} + \chi_2 D U_{xx} + E U_x) = O(\Delta x^3), \tag{8}$$

where

$$\begin{bmatrix} B = B(U), & & & \\ C = C\left(\varphi_1'', \varphi_2''^R, \varphi_2''^L, U, U_x\right) & \text{if } U_x \neq 0 & \text{at node } j \text{ (case 1)}, & \\ C \equiv 0 & \text{if } U_x = 0 & \text{at node } j \text{ (case 4)}, & \\ D = D(U, U_x), & & & \\ E = E(U, U_x), & & & \\ \chi_1 = 1 - 3\varphi_2' & \text{and } \chi_2 = 1 - \varphi_1' - \varphi_2' & \text{if } U_x \neq 0 \text{ at node } j, & \\ \chi_1 = 2 + \varphi_1 - \varphi_2 + 2\varphi_1' - 4\varphi_2' & \text{and } \chi_2 = 2 + \varphi_1 - \varphi_2 & \text{if } U_x = 0 \text{ at node } j. & \end{bmatrix}$$

Because of homogeneity between cases 1 and 4 (where $C \equiv 0$), the cancelation of C for case 1 gives the following condition on $\varphi'' = \frac{d^2\varphi}{dr^2}$:

$$\varphi_1''(1) = \varphi_2''^R(1) = \varphi_2''^L(1). \tag{9}$$

To avoid the appearance of numerical oscillations and to keep only the physical oscillations with higher wavenumbers (case 5 or 6), it is better to eliminate the dispersive error term BU_{xxx}. Although these oscillations are damped by the scheme, as we have seen in the previous paragraph, it is harmful to drop artificially the scheme accuracy if this is not necessary. Therefore, for cases 1 and 4, we let $\chi_1 = 0$. Applying conditions (6–7), we have

$$\varphi_2'(1) = \varphi_1'(1) = \frac{1}{3} \quad \text{if } U_x \neq 0 \text{ at nodes } j-1,\ j \text{ and } j+1 \text{ (case 1)}, \tag{10}$$

$$\varphi_2'(3) = 0 \quad \text{if } U_x = 0 \text{ at node } j \text{ (case 4)}. \tag{11}$$

5. LIMITER EXPRESSIONS

From conditions (6), (9), and (10) and the properties P_1 to P_5, it is possible to define a family of limiters φ_1 at each node j. φ_2^R and φ_2^L are expressed in the same way at points $j+1$ and $j-1$, respectively. At each point j, we define a *triad of limiters, each adapted to the local variation of the physical quantities*. If at node j we have

(i) case 1 ($r > 0$), we take limiter φ_{ATVL} defined in [1] as

$$\varphi_1 = \varphi_{ATVL} = \frac{1}{2}\left[(1-\kappa)\min\left(r, \frac{3-\kappa}{1-\kappa}\right) + (1+\kappa)\min\left(1, \frac{(3-\kappa)r}{1-\kappa}\right)\right] \quad \text{with } \kappa = 1/3 \tag{12}$$

(this is a third-order interpolation of $U_{j+1/2}^L$ and $U_{j-1/2}^R$ when r is closed to 1);

(ii) cases 2 and 3 ($r > 0$), we choose the least dissipative limiter to develop the energy cascade (property (P_3))

$$\varphi_1 = \varphi_{\text{cent}} = 1 \text{ (centered interpolation, no TVD scheme);} \tag{13}$$

(iii) case 4 ($r \le 0$), we define

$$\varphi_1 = 0; \tag{14}$$

(iv) cases 5 and 6, φ has to verify only the constraint (P_5).

The selected triad of limiters φ_{triad} is plotted in Fig. 2. This selection is not unique and other choices of limiters could be made.

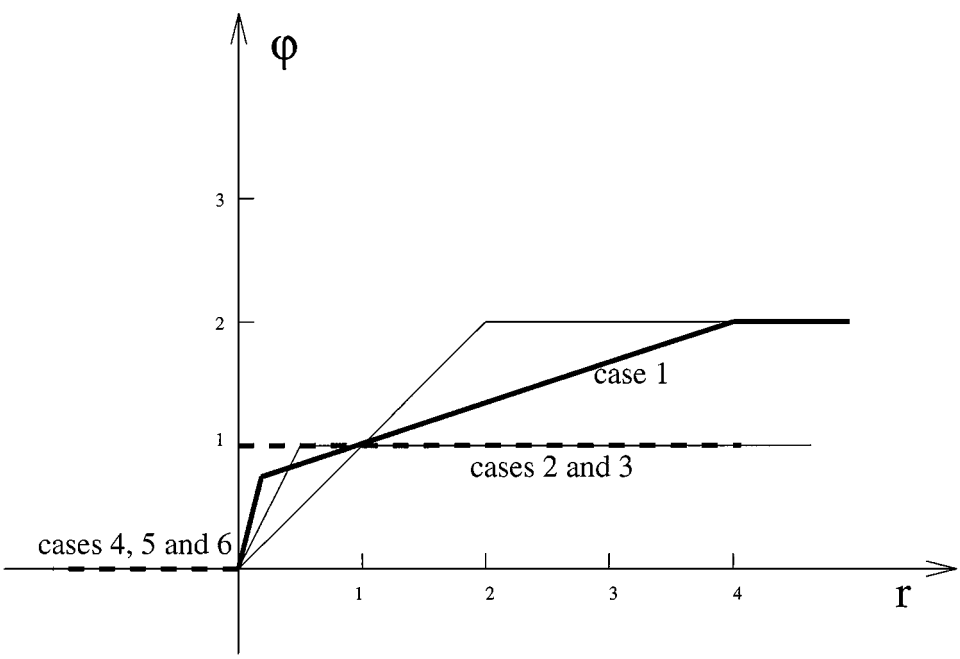

FIG. 2. Selected triad of limiters.

Algorithmically, the correction proposed herein is easy to implement and the additional time consumed is very small. The new encoding is summarized hereafter.

The expressions (3) are rewritten as

$$
\begin{aligned}
U^L_{j+1/2} &= U_j + \frac{1}{4}[(1-\kappa_j)\Delta_{-j} + (1+\kappa_j)\Delta_{+j}],\\
U^R_{j+1/2} &= U_{j+1} - \frac{1}{4}[(1-\kappa_{j+1})\Delta_{+_{j+1}} + (1+\kappa_{j+1})\Delta_{-_{j+1}}],\\
\Delta_{+j} &= \mathrm{Max}[0, \mathrm{Min}(A, \omega_j B)]\ \mathrm{sgn}(\delta U)_{j+1/2},\\
\Delta_{-j} &= \mathrm{Max}[0, \mathrm{Min}(B, \omega_j A)]\ \mathrm{sgn}(\delta U)_{j-1/2},\\
A &= \delta U_{j+1/2}\ \mathrm{sgn}(\delta U)_{j-1/2},\\
B &= \delta U_{j-1/2}\ \mathrm{sgn}(\delta U)_{j+1/2},\\
\delta U_{j+1/2} &= U_{j+1} - U_j.
\end{aligned}
$$

This set of equations is well known [24]. For example, with the limiter Superbee [15], $\omega_j = 2$ and $\kappa_j = \dim(\mathrm{sgn}(\delta U_{j+1/2}), 0) - \dim(0,\ \mathrm{sgn}(\delta U_{j+1/2}))$ and with the limiter φ_{ATVL} [1], $\omega_j = (3-\kappa_j)/(1-\kappa_j)$ and $\kappa_j = 1/3$. dim(. , .) is the FORTRAN intrinsic function.

About the φ_{triad}, we have

$$
\begin{aligned}
\omega_j &= \left(\frac{3-\kappa_j}{1-\kappa_j+\varepsilon}\right) i_2 + (1-i_2),\\
\kappa_j &= \frac{i_4}{3} + (1-i_4) i_2,\\
i_2 &= \frac{1}{2} iabs[\mathrm{sgn}(\delta U)_{j-1/2} + \mathrm{sgn}(\delta U)_{j+1/2}],\\
i_4 &= \frac{1}{4} iabs[\mathrm{sgn}(\delta U)_{j-3/2} + \mathrm{sgn}(\delta U)_{j-1/2} + \mathrm{sgn}(\delta U)_{j+1/2} + \mathrm{sgn}(\delta U)_{j+3/2}],
\end{aligned}
$$

where *iabs* is the FORTRAN intrinsic function and $\varepsilon \to 0$. These expressions for ω_j and κ_j are the only modifications introduced in the code.

From these expressions, we can summarize the values of ω_j and κ_j in the following table:

Case 1	$\omega_j \approx \frac{3-\kappa_j}{1-\kappa_j}$	$\kappa_j = \frac{1}{3}$
Case 2 and 3	$\omega_j \to \infty$	$\kappa_j = 1$
Case 4, 5, and 6	$\omega_j = 1$	$\kappa_j = 0$

Although ω_j and κ_j take the same values for cases 4, 5, and 6, the scheme does not degenerate into first order automatically, in particular for case 4 because accuracy also depends on the values of these both parameters at nodes $j-1$ and $j+1$.

6. NUMERICAL RESULTS

The triad of limiters plotted in Fig. 2 is tested on Euler and Navier–Stokes equations. It is applied to the 1-D simulation proposed by Shu and Osher [18] to simulate the interaction between a moving shock wave and a fluctuating flow. A 2-D simulation of the interaction between a weak shock and a spot of temperature is proposed. Two cases with

freely decaying isotropic turbulence following the MILES approach [2] are also performed: a quasi-incompressible case and a compressible case. Computations of viscous flows as the advection of a Taylor vortex and 2-D and 3-D temporal compressible mixing layers are presented. The viscous terms are solved with a second-order centered scheme and the time integration is performed by means of the following second-order scheme:

$$\begin{aligned} \tilde{V}_j &= V_j^n - \sigma(F_{j+1/2} - F_{j-1/2}), \\ V_j^{n+1} &= \frac{1}{2}\left[(V_j^n + \tilde{V}_j) - \sigma(\tilde{F}_{j+1/2} - \tilde{F}_{j-1/2})\right]. \end{aligned} \tag{15}$$

For the multidimensional problems, a time-splitting method is used [19, 23]. The 2-D and 3-D finite difference operators are split into a product of simpler operators (e.g., for a 2-D problem):

$$V_j^{n+2} = \left(\pounds_x\left(\frac{\Delta t}{2}\right)\pounds_y\left(\frac{\Delta t}{2}\right)\pounds_y\left(\frac{\Delta t}{2}\right)\pounds_x\left(\frac{\Delta t}{2}\right)\right)V_j^n.$$

$\pounds_x$ and $\pounds_y$ are the 1-D difference operators in spatial directions x and y associated with the scheme (15).

6.1. *Shu–Osher Test Case*

In 1-D, this example is interesting because it uses the Euler equations to simulate the interaction between a moving Mach 3 shock wave and a fluctuating flow represented by sine waves in density. The initial conditions are described as

$$\begin{aligned} &\rho = 3.857143, \quad u = 2.629369, \quad p = 10.33333 \quad \text{if } -5 \le x < -4, \\ &\rho = 1 + 0.2\sin 5x \quad u = 0, \quad p = 1 \quad \text{if } 5 \ge x \ge -4. \end{aligned}$$

The CFL number is equal to 0.5 and the final time is $t = 1.8$. Since the exact solution for this problem is unknown, the solid line representing the numerical solution with 1600 cells is assumed to be the exact solution.

Figures 3a–3c show the solution of the density field with 400 cells and the limiters φ_{minmod} (the most dissipative of TVD second-order area), $\varphi_{superbee}$ (the least dissipative of TVD second-order area), and φ_{ATVL}. The limiters φ_{minmod} and $\varphi_{superbee}$ give middling solutions. φ_{minmod} damps the fluctuations and, at the opposite end, $\varphi_{superbee}$ enhances unphysical amplitudes. The results are better with φ_{ATVL} but it is still too diffusive. If φ_{triad} is applied (Fig. 3d), the solution is comparable to that of the third-order ENO scheme [18]. In particular, the high frequencies are well represented and the compression waves and the shock are well captured.

6.2. *Spot of Temperature–Shock Interaction*

This configuration is a basic model for the interaction of a shock with a flame. Euler equations are solved. The computational domain (x, y) has a dimension 4×1. A uniform grid with 401×101 points is used and $CFL = 0.5$. The plane weak shock is located at $x_s = 1$. The prescribed pressure jump through the shock is $\Delta p/p_\infty = 0.4$, where p_∞ is the static pressure at infinity, corresponding to a Mach number $M = 1.1588$. The flow is

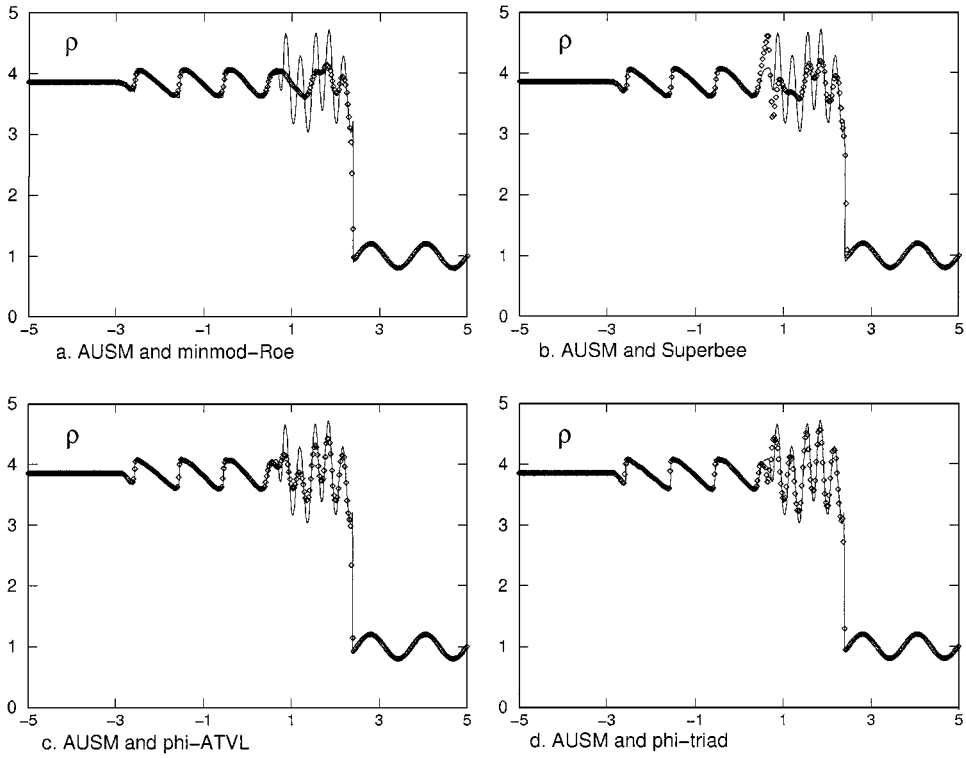

FIG. 3. Shu–Osher test case. Density distributions at $t = 1.8$.

initialized using the Rankine–Hugoniot relationships. Initially, the spot of temperature has a top-hat shape and is surperposed on the base flow upstream of the shock. It is defined as

$$\frac{\Delta T}{T} = \frac{1}{2}[3 + \tanh 100(0.2 - r)],$$

with $r = \sqrt{(x - x_0)^2 + (y - y_0)^2}$, and $x_0 = 0.5$, $y_0 = 0.5$ are the coordinates of the initial location of the center of the spot. The pertubation of temperature is supposed to be isobaric. Periodic conditions are applied on the upper and lower boundaries. The initial temperature field is presented in Fig. 4a. This interaction produces vorticity through two counter-rotating vortices. At $t = 3$, the spot is far from the shock and the vorticity, concentrated in the core of the vortices, cancels within the shock. With the classical limiters (e.g., φ_{ATVL}), the vorticity field is not smooth and some irregularities are visible in the shock and behind the spot (Fig. 4b). With φ_{triad}, these problems dissappear (Fig. 4c). On these two last figures, 20 vorticity contours are plotted with $\omega_{max} = 3$ and $\omega_{min} = -3$. The longitudinal vorticity distribution at $y = 0.64$ (line where the maximum value is located) is plotted for both limiters. The vorticity level is better kept with φ_{triad} and the numerical oscillations through the shock are nearly canceled (Fig. 5).

6.3. *Freely Decaying Isotropic Turbulence*

For this test case, the Euler equations are again solved. The simulations are performed in a cube of edge length 2π with 65^3 uniformly distributed grid points. The boundary conditions

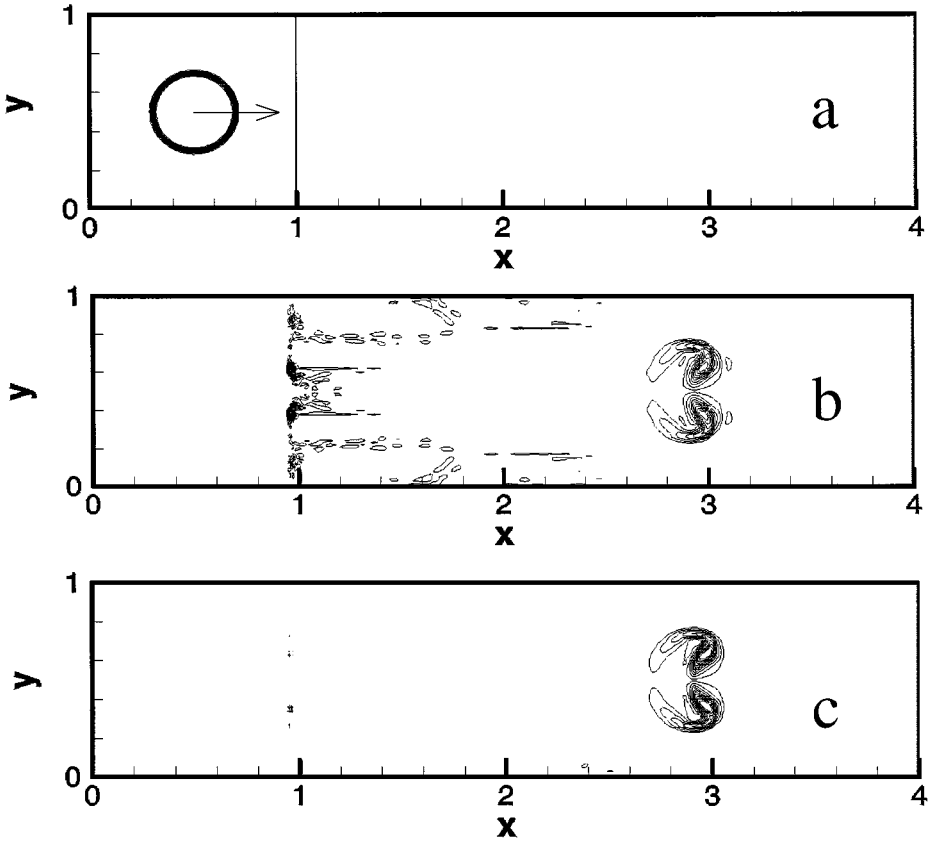

FIG. 4. (a) Initial temperature field, (b) vorticity field at $t = 3$ with φ_{ATVL}, and (c) vorticity field at $t = 3$ with φ_{triad}.

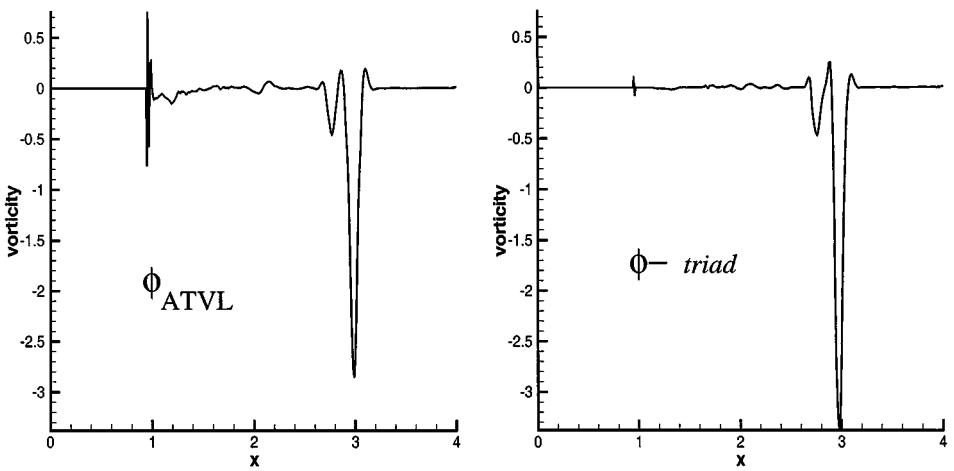

FIG. 5. Longitudinal distribution of vorticity for $y = 0.64$ at $t = 3$.

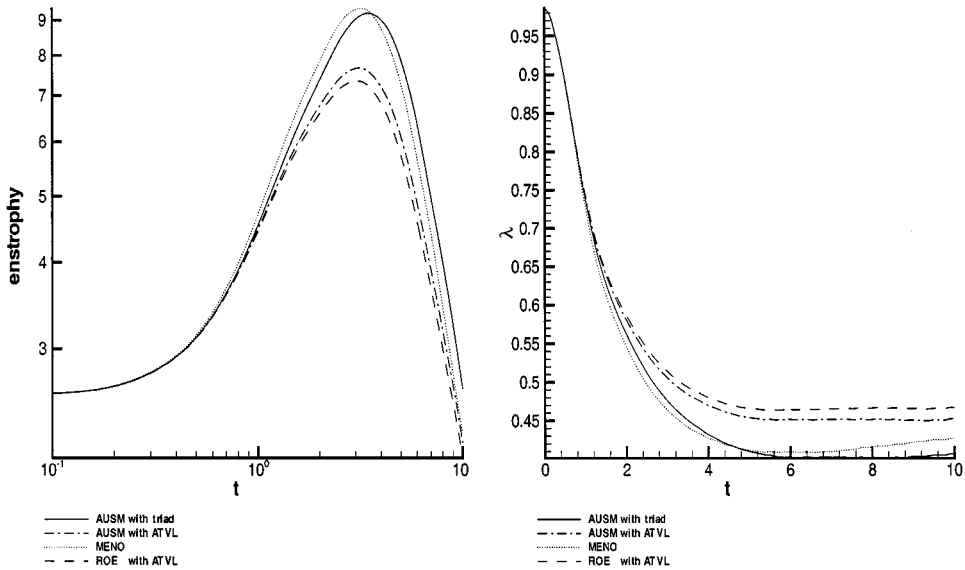

FIG. 6. Time evolution of enstrophy and Taylor microscale, case C1.

are periodic in the three directions. Two cases studied in [4] are:

- a quasi-incompressible case (C1): initial rms Mach number $M_{\text{rms}} = 0.2$ and initial compressibility ratio $\chi = 0$,
- a sonic compressible case (C2): $M_{\text{rms}} = 1$ and $\chi = 0.05$,

where

$$M_{\text{rms}} = \frac{u_{\text{rms}}}{c} = \frac{\sqrt{\overline{u'^2}}}{c} \quad \text{and } x = \frac{\varepsilon_c}{\varepsilon},$$

where $\mathcal{E}_c$ is the compressible part of the spectrum energy $\mathcal{E}$ [4]. Overbars indicate the spatial average. The initial velocity fields have power-law spectra $\sim k^4 e^{-2(k^2/k_0^2)}$ with $k_0 = 2$. The computations are carried out up to $t = 10$, which corresponds to three initial eddy turn-over times. The time step has a fixed value. The corresponding CFL numbers vary between 0.5 and 0.4 for C1 and between 0.3 and 0.2 for C2.

6.3.1. The quasi-incompressible case. As explained in [8], at large but finite *Re*, the evolution of freely decaying incompressible isotropic turbulence follows two different stages. During the first one, the viscous effects are negligible, the flow develops strongly anisotropic phenomena, and enstrophy increases dramatically because of vortex stretching. Afterward, viscous effects begin to appear and play a major role on the creation of distorted dissipative structures. The two stages are represented in Fig. 6, where the enstrophy is plotted versus time. The results obtained with AUSM-φ_{triad} are compared with three other schemes:

- a two-time-step scheme (15) using AUSM splitting and the third-order limiter φ_{ATVL} which corresponds to the case 1 in Fig. 2,
- Roe TVD scheme with φ_{ATVL} using a four-stage Runge–Kutta time marching technique [4],
- a fifth-order-accurate in space MENO scheme using a three-stage Runge–Kutta TVD time marching technique [4].

The schemes AUSM-φ_{ATVL} and Roe-φ_{ATVL} give about the same results, with a slightly better performance for AUSM-φ_{ATVL}. Use of φ_{triad} allows improvement of the behavior of

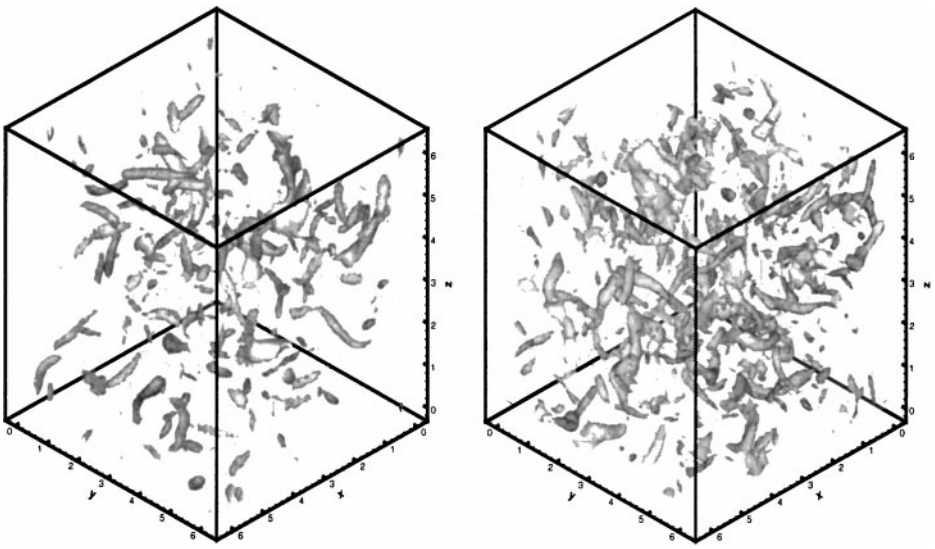

FIG. 7. Iso-surfaces of a constant value of vorticity at $t = 10$, AUSM-φ_{ATVL} (left) and AUSM-φ_{traid} (right), case C1.

the complete algorithm and comparison with equivalent results from MENO. The evolution of both the curves is similar but with a time delay on the appearance of the peak of enstrophy.

The Taylor microscale λ, characteristic of the mean spatial extension of the velocity gradients, is used to measure the resolved gradients with the numerical algorithms. Figure 6 presents the time evolution of λ for the four schemes. Again, the best results are obtained with MENO and AUSM-φ_{triad}. Particularly, AUSM-φ_{triad} gives, at $t = 10$, the smallest value of λ. At this time, the respective values of λ based on the mesh size Δx are summarized in this table:

Roe-φ_{ATVL}	AUSM $-$ φ_{ATVL}	MENO	AUSM-φ_{triad}
$4.7\Delta x$	$4.6\Delta x$	$4.3\Delta x$	$4.0\Delta x$

The schemes have to reproduce the basic mechanisms of turbulence such as vortex stretching and the elongated structures called "worms." Figure 7 shows the contours of vorticity at $t = 10$ for schemes AUSM-φ_{ATVL} and AUSM-φ_{triad}. The chosen value is fixed at $2(\overline{\omega}^2)^{1/2}$ where ω is the local vorticity. These schemes reproduce the worms as in spectral DNS simulations but AUSM-φ_{triad} gives a finer representation of these structures. Nevertheless, for this case, the dissipation is still too high, particularly for wavenumbers $k > 10$ (Fig. 8). If a centered interpolation is used for the MUSCL approach ($\varphi = 1, \forall r$), the kinetic energy spectrum is proportional to k^2 (Fig. 9) as found in [7] during a lapse of time just before the computation blows up. The scheme is no longer sufficiently dissipative to attenuate the accumulation of energy at the greatest wavenumbers. But if a correct SGS model (Smagorinsky model) is coupled with this AUSM-centered scheme, the theoretical $-5/3$ slope is obtained (Fig. 9).

6.3.2. The compressible case. This case looks like the one studied in [12], where $M_{\text{rms}} = 1.0$ and $\chi = 0.068$. With a PPM scheme and a high grid resolution (512^3), the authors distinguished three different temporal phases: an onset phase with the appearance of shocks at its end ($0 \leq t \leq 0.95$, the time scale has to be divided by π to fall back on the scale used

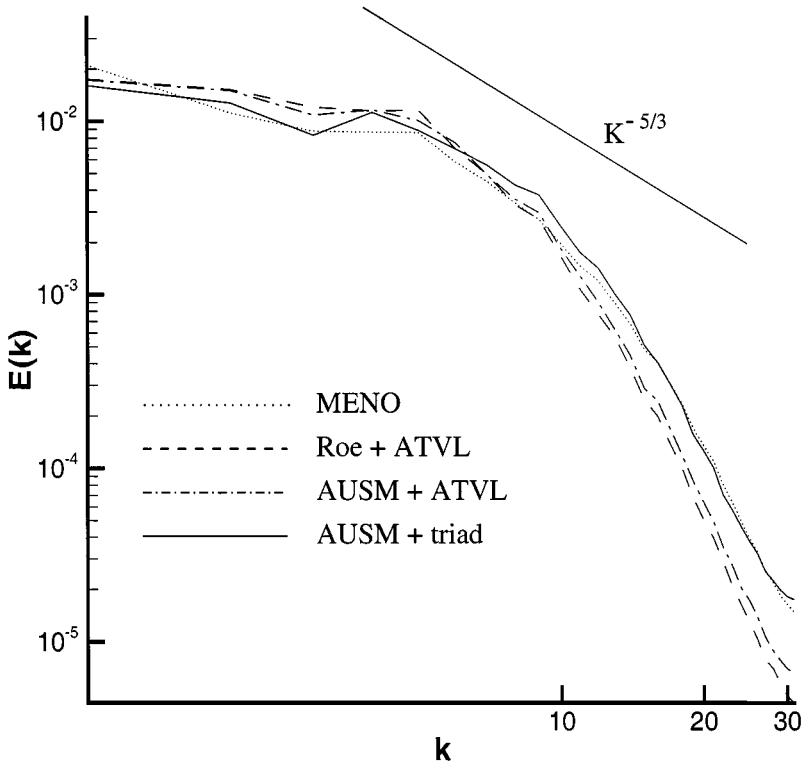

FIG. 8. Kinetic energy spectrum at $t = 10$, case C1.

in [12]), a supersonic phase with the setup of strong density contrasts $\rho_{\max}/\rho_{\min}(0.95 \leq t \leq 6.6)$, and a post-supersonic phase with a presence of vortex interactions and the vortical decay. The three phases are visualized in Fig. 10, where the time evolution of the density contrast is plotted for MENO and AUSM-φ_{triad} schemes. The evolutions are close to those found in [12] and the physical trends are reproduced.

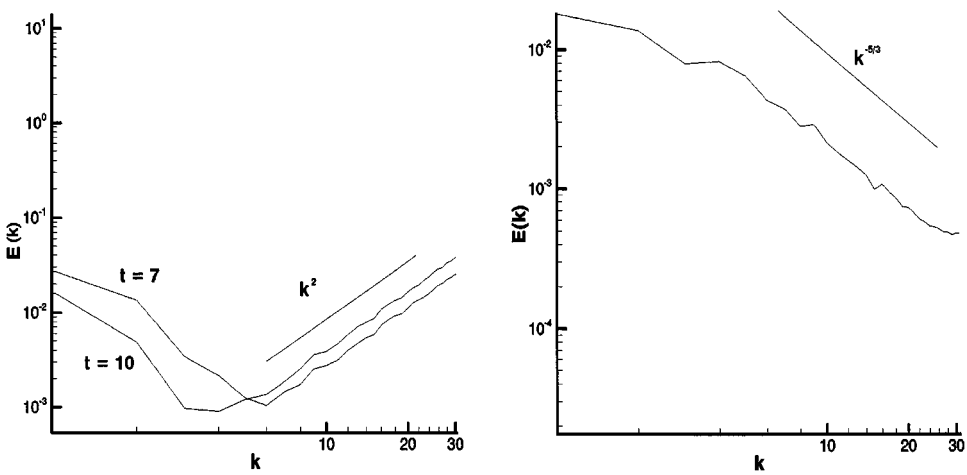

FIG. 9. Kinetic energy spectrum with a centered scheme without (left) and with a Smagorinsky model (right) at $t = 10$, case C1.

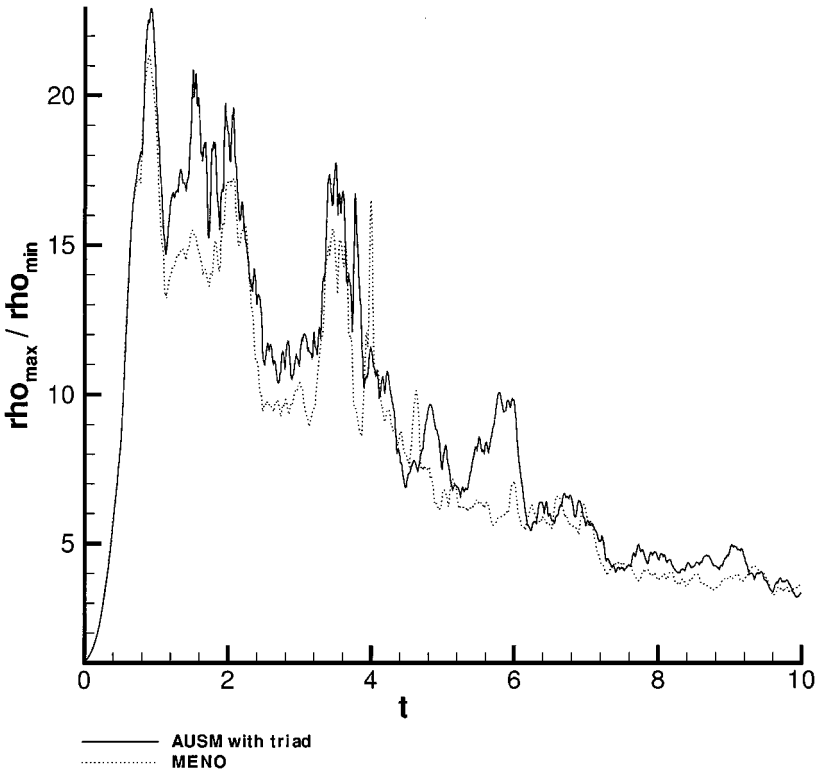

FIG. 10. Time evolution of density contrast, case C2.

The time history of the kinetic energy plotted on Fig. 11 shows that AUSM-φ_{triad} retains more energy than the others along the second and the third stages. In particular, it preserves more compressible energy $\mathcal{E}_c$ for $t \geq 1$, the time where the spectrum of compressible energy begins to be saturated (Fig. 11).

6.4. *Taylor Vortex Advection*

The squared domain (x, y) has a dimension 1×1 and Navier–Stokes equations are solved. A uniform grid with 201^2 points is employed and CFL $= 0.5$. An isolated Taylor vortex is initially superposed on a uniform flow with a Mach number $M = 0.8$ and a Reynolds number $Re = 10^4$. The tangential velocity is given by

$$V_\theta(r) = C_1 r e^{-C_2 r^2},$$

with

$$C_1 = \frac{0.3}{r_c} e^{1/2}, \quad C_2 = \frac{0.5}{r_c^2}, \quad r = \sqrt{(x - x_0)^2 + (y - y_0)^2}, \quad \text{and} \quad r_c = 0.075.$$

With these values, the viscous core radius is $1/2$. The initial position of the vortex center is $x_0 = 0.5$, $y_0 = 0.5$. Periodic conditions have been applied in both directions on the boundaries.

The simulation is performed over a dimensionless time $t = 5$, corresponding to the advection of the vortex over five lengths of the domain. Because of the effects of both molecular viscosity and numerical diffusion, the viscous core radius is a growing function

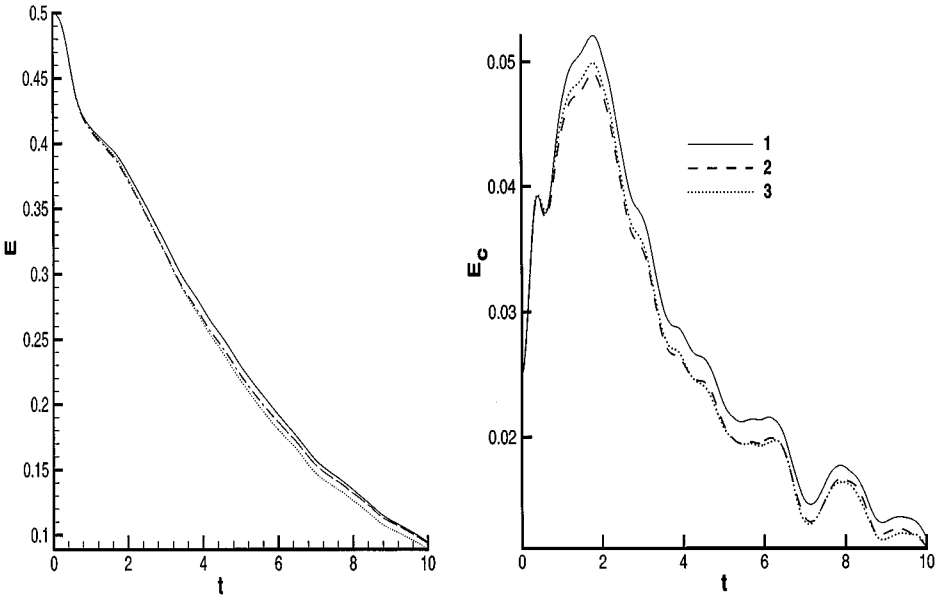

FIG. 11. Time evolution of energy decay (left) and compressible energy decay (right) (1 = AUSM-φ_{triad}, 2 = AUSM-φ_{ATVL}, 3 = MENO), case C2.

of time. The pressure defect is located in the center of the vortex. The results obtained with φ_{triad} are compared with those obtained with a sixth-order-accurate Hermitian scheme on the same grid. It can be noted in Fig. 12 that the AUSM-φ_{triad} scheme gives results in very good agreement with the Hermitian scheme. To get a finer analysis of the capability of the AUSM-φ_{triad} scheme, a zoom around the center of the vortex is provided on the longitudinal distributions of v and p.

6.5. *2-D Time-Developing Mixing Layer*

This test case consists of two streams moving in the opposite directions, with a smooth velocity profile in between:

$$u = \frac{1}{2}\tanh(2y).$$

The mean temperature profile is

$$T = 1 + M^2\frac{\gamma - 1}{2}(1 - u^2), \tag{16}$$

with $M = 0.8$ and $\gamma = 1.4$. The flow is periodic in the streamwise direction, x, and symmetry conditions are applied in the normal direction, y. The mesh is uniform in both directions. The computations are realized on two grids (150^2 cells ($G1$) and 300^2 cells ($G2$)).

This flow is sensitive to small disturbances, and so the instability is forced by adding small perturbations u' and v' to the mean flow,

$$\begin{cases} u' = \frac{\alpha y L_x}{10\pi}\sin\left(\frac{2\pi x}{L_x}\right)e^{-\frac{y^2}{10}} \\ v' = \alpha\cos\left(\frac{2\pi x}{L_x}\right)e^{-\frac{y^2}{10}}, \end{cases}$$

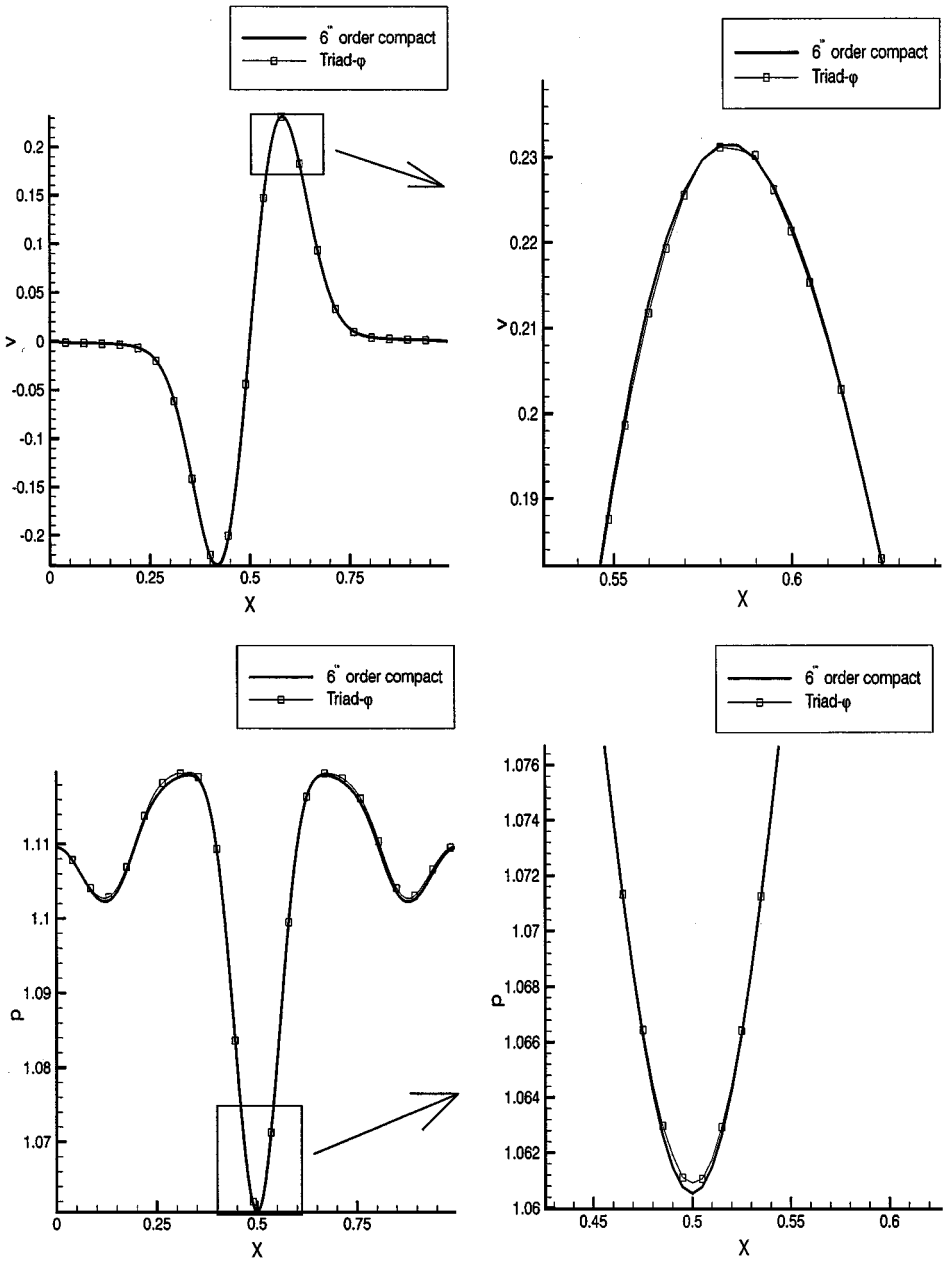

FIG. 12. Taylor vortex advection: longitudinal distribution along the centerline of the domain of the velocity component v (top) and the static pressure p (bottom) at $t = 5$.

with amplitude $\alpha = 0.05$ and wavelength $L_x = 20\delta_{\omega 0}$, where $\delta_{\omega 0} = 1$ represents the initial vorticity thickness. The height of the domain is $L_y = 26$. The vorticity thickness is defined as

$$\delta_\omega = \frac{\Delta u}{\left| \frac{d\left(\frac{\overline{\rho u}}{\overline{\rho}}\right)}{dy} \right|_{\max}},$$

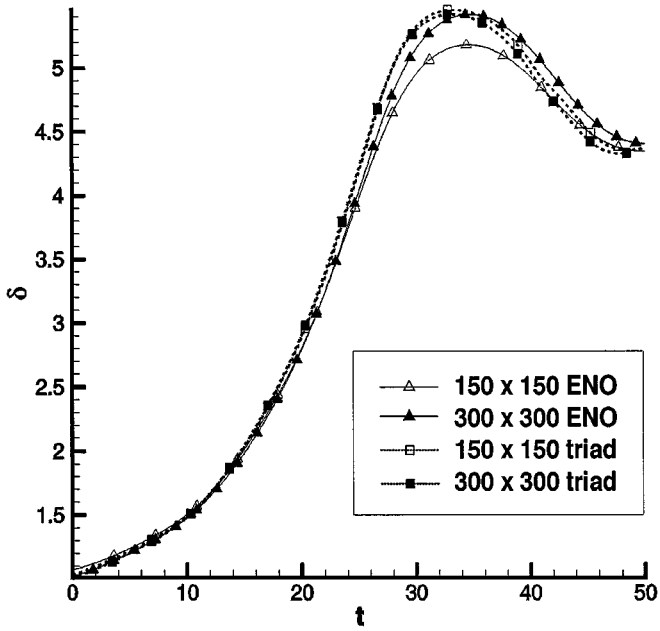

FIG. 13. 2-D mixing layer. Time evolution of vorticity thickness.

where Δu is the difference between the velocities in the upper and lower domains. $\overline{\rho}$ and $\overline{\rho u}$ are spatial averages in the x-direction. Two-dimensional Navier-Stokes equations are solved. The convective Mach numbers is $M_c = 0.38$, the Reynolds number is $Re = 400$ and $CFL = 0.5$. The growth history of the mixing layer is shown in Fig. 13 and compared with ENO computations under the same initial conditions. The ENO scheme is still sensitive to the grid mesh, whereas the AUSM-φ_{triad} scheme is already independent. AUSM-φ_{triad} gives a result with 150^2 cells similar to that of ENO with 300^2 cells. The only difference is located in the nonlinear phase where the growth of δ_ω is faster with AUSM-φ_{triad}. Five vorticity contours obtained on the grid $G1$ with AUSM-φ_{ATVL}, AUSM-φ_{triad}, and ENO schemes are plotted in Fig. 14. The differences are weak in the vortex but AUSM-φ_{triad} has a best behavior in the braid.

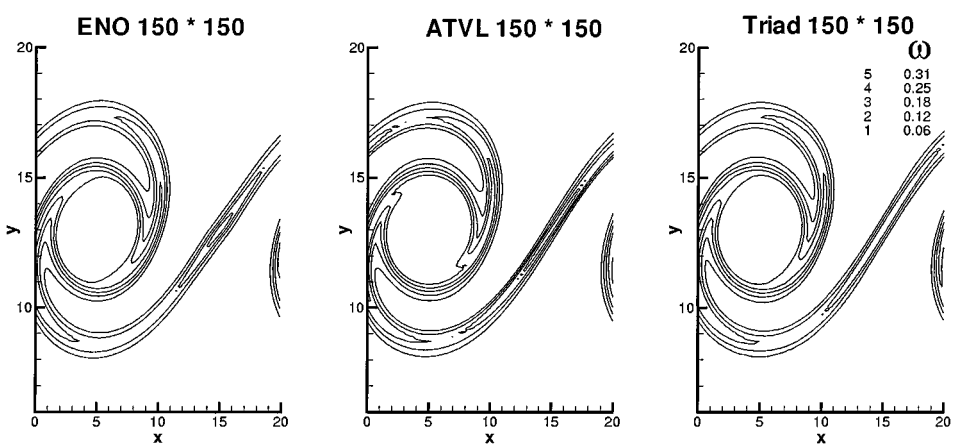

FIG. 14. 2-D mixing layer. Iso-vorticity at t = 50.

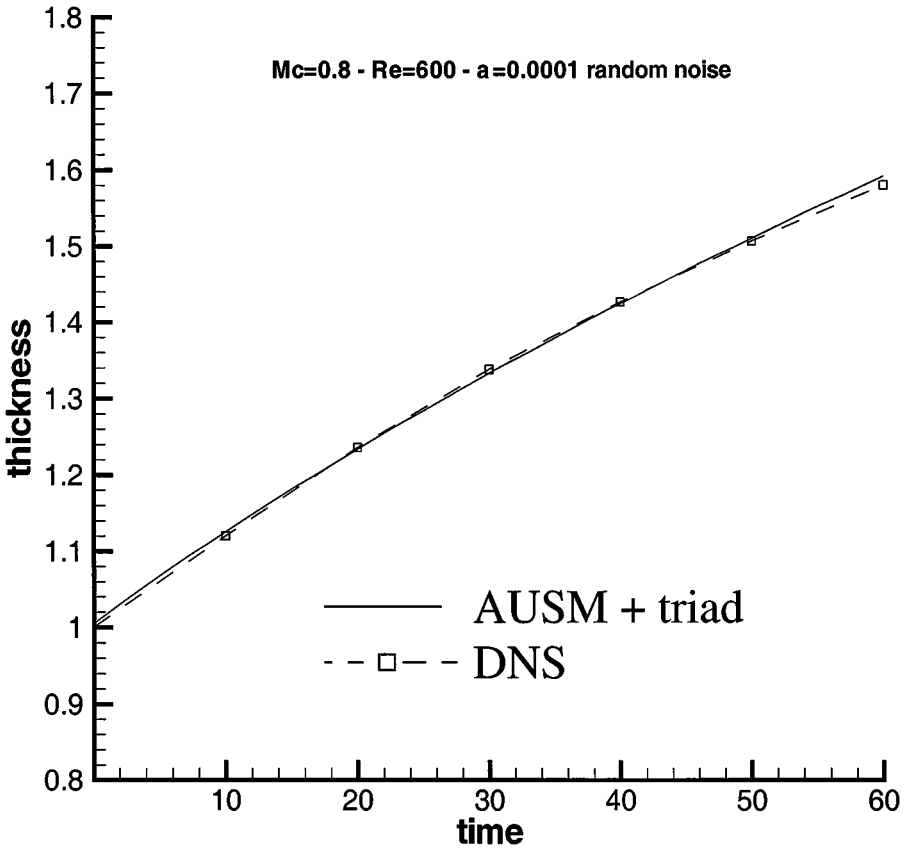

FIG. 15. 3-D mixing layer. Time evolution of vorticity thickness (computation C_1).

6.6. *3-D Time-Developing Mixing Layer*

As in the previous case, Navier–Stokes equations are solved. The results of AUSM-φ_{triad} scheme are compared with the results of a DNS computation. The initial conditions are defined in [16]. The essential conditions of the computation are rewritten here: the domain has a parallelepipedic shape with 65 grid points uniformly spaced in each direction. The box lengths are $L_x = L_z = 13.36$ and $L_y = 10$. Periodicity conditions are imposed in x and y directions and a slip condition is applied on the walls bounding the domain in the z-direction. The mean velocity profile is given by

$$u = \mathrm{erf}(y\sqrt{\pi})$$

and the temperature profile has the expression (16). The static pressure is uniform, $Re = 600$, $M_c = 0.8$, and $CFL = 0.5$. The initial conditions are specified by adding a small random number to each quantity (ρ, u, v, w, T). For example,

$$\rho(x, y, z) = \rho(x, y, z) + \alpha r \exp^{-y^2},$$

where $\alpha = 0.0001$ (computation C_1) or 0.0025 (computation C_2) and r is a random number uniformly distributed between -0.5 and 0.5.

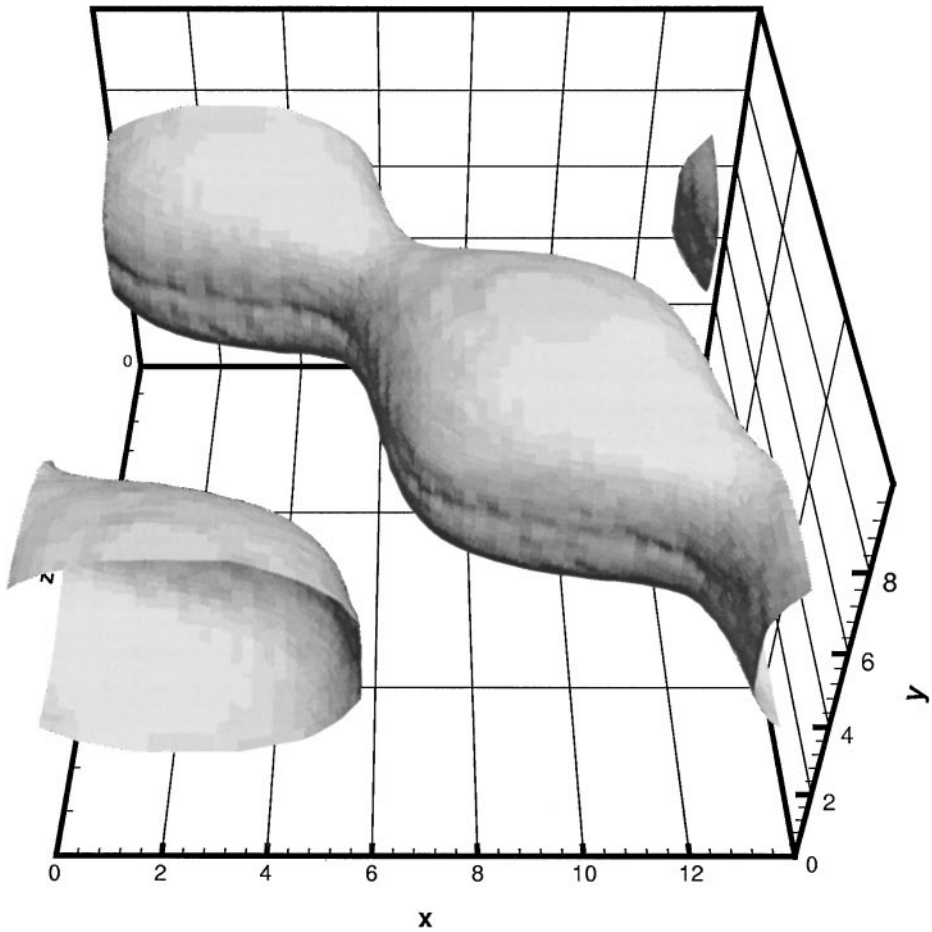

FIG. 16. 3-D mixing layer. One static pressure surface at $t = 45$ (computation C_2).

The time-developing mixing layer follows three phases. The first one corresponds to the linear growth of the fundamental, most unstable mode. The second one describes the nonlinear setup (growth of the subharmonic waves) and the last one describes saturation. The time evolution of the thickness vorticity during the linear phase is plotted on Fig. 15 (computation C_1) and compared with the result obtained in [16] with a direct numerical simulation.

After Sandham and Reynolds [16], with an initial disturbance of the form

$$u' = \hat{u} \exp^{i(\beta x + \gamma z - \omega t)},$$

where β and γ are the wavenumbers in x- and z-directions respectively and $\hat{u}$ is an eigenfunction of the linear instability wave, the oblique mode is the most amplified when $0.6 < M_c < 0.8$. The behavior of the flow becomes strongly 3D. The results of this simulation are presented in Figs. 16 and 17 (computation C_2). One static pressure contour value is shown at $t = 45$ (linear phase) and at $t = 65$ (starting of the nonlinear phase). At $t = 45$, the minimum and the maximum values of p are $p_{\min} = 1.0146$ and $p_{\max} = 1.0163$ and the plotted value of the surface is $p_{plotted} = 1.0156$. At $t = 65$, $p_{\min} = 0.8482$, $p_{\max} = 1.115$, and $p_{plotted} = 0.95$. As explained in [16], when $M_c = 0.8$, during the linear phase, there is

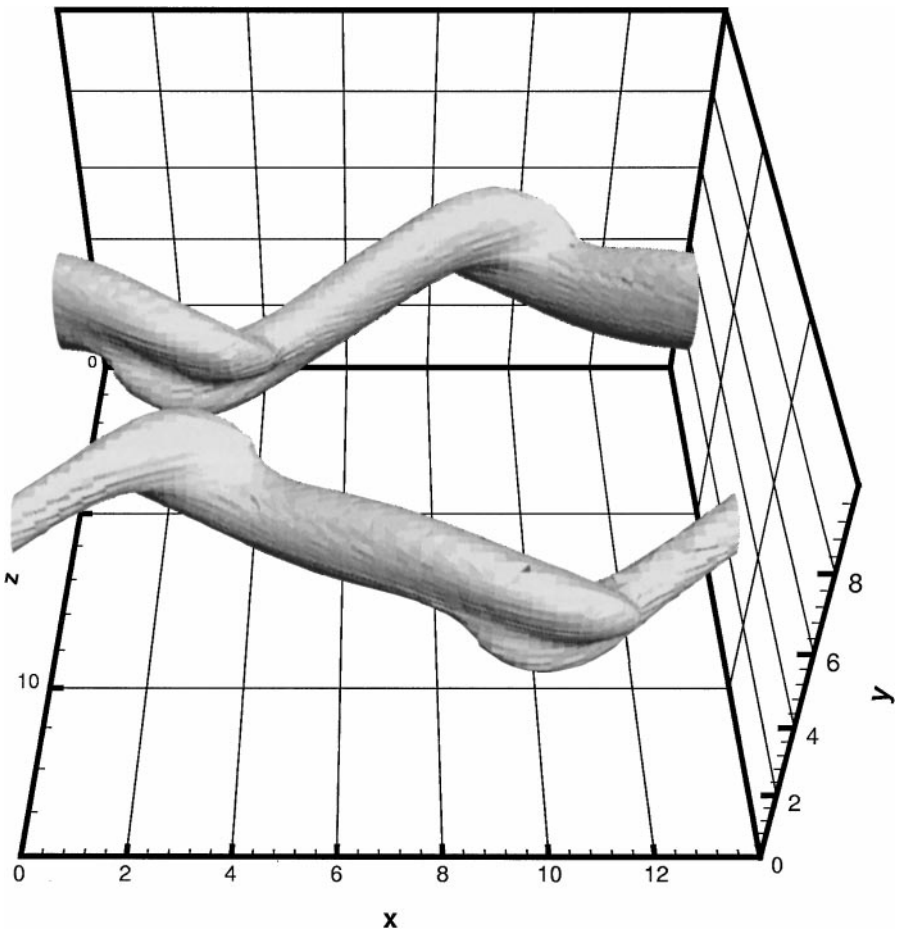

FIG. 17. 3-D mixing layer. One static pressure surface at $t = 65$ (computation C_2).

no longer any tendency toward a spanwise coherence and waves at 45° are most common. This behavior is well described by the scheme.

7. CONCLUSION

The test cases show that it is possible to improve the accuracy of the MUSCL approach. This becomes equivalent to ENO family schemes or Hermitian schemes for the compressible flows if the nonlinear functions φ are expressed in a φ_{triad} taking into account the local variations of each quantity. For the quasi-incompressible flows, an AUSM-centered scheme coupled with a SGS model seems to be a good approach. Adding to the basic well-known advantages of the algorithm proposed herein, the good accuracy of the numerical solution opens new perspectives for the schemes based on the MUSCL approach, particularly for simulations of unsteady or transient flows. Algorithmically, the correction proposed herein is easy to implement and the additional time consumed is very small. Other computations [5] show that the φ_{triad} associated with Roe splitting brings out the same improvements as the coupling AUSM-φ_{triad}.

REFERENCES

1. W. K. Anderson, J. L. Thomas, and B. van Leer, Comparison of finite volume flux vector splittings for the Euler equation, *AIAA J.* **24**, 1453 (1986).
2. J. P. Boris, F. F. Grinstein, E. S. Oran, and R. L. Kolbe, New insights into large eddy simulations, *Fluid Dyn. Res.* **10**, 199 (1992).
3. B. Cockburn and C.-W. Shu, Nonlinearly stable compact schemes for shocks calculations, *SIAM J. Numer. Anal.* **31**, 607 (1994).
4. E. Garnier. M. Mossi, P. Sagaut, P. Comte, and M. Deville, On the use of shock-capturing schemes for large-eddy simulation, *J. Comput. Phys.* **153**, 273 (1999).
5. L. Gozalo and R. Abgrall, A new limiter that improves TVD-MUSCL schemes, in *Godunov Methods: Theory and Applications*, edited by E. F. Toro (Kluwer Academic/Plenum, Dordrecht/New York, 2000).
6. C. Hirsch, *Numerical Computations of Internal and External Flows,* Vol. II (Wiley, New York, 1990).
7. T. D. Lee, On some statistical properties of hydrodynamical and magneto hydrodynamical fields, *Q. Appl. Math.* **10**, 69 (1952).
8. M. Lesieur, *Turbulence in Fluids* (Martinus Nijhoff, Dordrecht, 1987).
9. M. S. Liou and Ch. Steffen, A new flux splitting scheme, *J. Comput. Phys*. **107**, 23 (1993).
10. M. S. Liou, A sequel to AUSM: AUSM$^+$, *J. Comput. Phys.* **129**, 364 (1996).
11. R. Peyret, *Résolution numérique des systèmes hyperboliques. Application à la dynamique des gaz,* Publication ONERA, **5** (1977).
12. D. H. Porter, A. Pouquet, and P. R. Woodward, A numerical study of supersonic turbulence, *Theor. Comput. Fluid Dyn*. **4**, 13 (1992).
13. R. Radespiel and N. Kroll, Accurate flux vector splitting for shocks and shear layers, *J. Comput. Phys*. **121**, 66 (1995).
14. R. D. Richtmyer and K. W. Morton, *Difference Methods for Initial Value Problems* (Interscience, New York, 1967).
15. P. L. Roe, *Some Contributions to the Modelling of Discontinuous Flows,* Lecture Notes in Applied Mathematics (Springer-Verlag, Berlin/New York, 1985), Vol. 22.
16. N. D. Sandham and W. C. Reynolds, Three-dimensional simulations of large eddies in the compressible mixing layer, *J. Fluid Mech*. **224**, 133 (1991).
17. C.-W. Shu and S. Osher, *Efficient Implementation of Essentially Non-Oscillatory Shock-Capturing Schemes*, *J. Comput. Phys.* **77**, 439 (1988).
18. C.-W. Shu and S. Osher, *Efficient implementation of Essentially Non-Oscillatory Shock-Capturing Schemes, II*, CAM Report 88-12, UCLA (1988), pp. 506–517.
19. W. G. Strang, On the construction and comparison of difference schemes, *SIAM J. Numer. Anal*. **5**, 3 (1968).
20. P. K. Sweby, High resolution scheme using flux limiters for hyperbolic conservation laws, *SIAM J. Numer. Anal*. **21**, 995 (1984).
21. B. van Leer, Towards the ultimate conservative difference scheme. V. A second-order sequel to Godunov's method, *J. Comput. Phys.* **32**, 101 (1979).
22. B. van Leer, Flux vector splitting for the Euler equations, in *Proceedings of 8th International Conference on Numerical Methods in Fluids Dynamics* (Springer-Verlag, Berlin 1982).
23. N. N. Yanenko, A difference method of solution in the case of the multidimensional equation of heat conduction, *Dokl. Akad. Nank SSR* **125** (1959).
24. H. C. Yee, *Upwind and Symmetric Shock-Capturing Schemes*, NASA Technical Memorandum 89464 (1987), pp. 1207–1210.